Validating 3D two-parameter fracture mechanics models for structural integrity assessments

C.A. Simpson[a]*, S. Tonge[a], T Connolley[b], C. Reinhard[b], T.J. Marrow[c], M. Mostafavi[a]

[a] *Department of Mechanical Engineering, University of Bristol, University Walk, Bristol, BS8 1TR, UK*
[b] *Diamond Light Source, Harwell Science & Innovation Campus, Didcot OX11 0DE, UK*
[c] *Department of Materials, University of Oxford, Oxford OX1 3PH, UK*

Abstract

In-situ fracture tests were carried out on the I12 beamline at the Diamond Light Source. Four Al-Ti metal-matrix composites (MMCs), with two crack lengths, were studied to assess for the impact of in-plane constraint. Synchrotron X-ray computed tomography and synchrotron X-ray diffraction were used to measure total strain and elastic strain respectively. In this work, the measured elastic strains in the samples are detailed as a function of applied load and compared against those predicted from a 3D elastic-plastic finite element model. The modelled strains increased asymptotically towards the tip of the electro discharge machined notch. The experimental results do not highlight the same response, which is due to a combination of blunting and low experimental spatial resolution. Far field experimental and measured strain fields converged, notably in the test piece containing a long notch (a/W = 0.5) and higher levels of constraint.

Peer-review under responsibility of the ECF22 organizers.

Keywords: strain energy release rate; J-integral; plastic constraint; XRD; XCT; DVC; DIC

1. Introduction

Understanding the impact of constraint on fracture behaviour is central to the accurate, non-conservative life assessment of safety critical structural components used in the aerospace and nuclear industries. The fracture resistance of cracked bodies with low levels of plastic constraint is significantly under-estimated when using a single parameter fracture assessment. Attempts are therefore made to account for the impact of constraint in integrity assessment codes such as UK's R6 using fracture parameters such as T (Larsson & Carlsson, 1973), Q (O'Dowd & Shih, 1991) and Tz (Mu, Wang, Tu, & Xuan, 2016). These parameters are, however, only sensitive to either in-plane (T, Q) or out-of-plane (Tz) constraint. There is therefore a need to improve on the current methodology and move towards a simple, unified parameter that better addresses both in-plane and out-of-plane constraint. Recently there have been promising advances, with authors such as Mostafavi et al. (Mostafavi, Smith, & Pavier, 2010), Yang et al. (2013) and Seal & Sherry (2017) detailing parameters that capture the extent or volume of plasticity around the crack tip as a function of constraint. While these parameters have been shown to be sensitive to both in-plane and out-of-plane constraint, there is still more fundamental research required to properly quantify and validate the dependence of fracture toughness on 3D plastic constraint (i.e. loss of both in-plane and out of plane constraint). To that end, we have used a novel

* Corresponding author.
E-mail address: c.simpson@bristol.ac.uk

2452-3216
Peer-review under responsibility of the ECF22 organizers.

combination of synchrotron X-ray diffraction (XRD), X-ray computed tomography (XCT) and finite element analysis (FEA) to study and separate the elastic and plastic contributions to strain energy release rate with respect to both 3D plastic constraint and through thickness position. The following work details both the methodology used and some of the initial results, concentrating on the study and validation of elastic strain measurements using synchrotron X-ray diffraction. These results are compared against those from a 3D finite element model, with the goal being to (a) validate this model and (b) ultimately use the finite element model to extract parameters such as the T-stress (for validation and comparison against existing models) and for the calculation of the elastic portion of the strain energy release rate, $J_{elastic}$ with respect to 3D constraint. High energy X-ray diffraction provides us with a unique opportunity to experimentally validate the effect of 3D constraint and interrogate models and approaches that have previously been solely subject to systematic finite element studies.

Nomenclature

2θ Bragg angle (°)
α, n Ramberg-Osgood hardening coefficients
a crack length (mm)
b, W sample thickness and width (mm)
d, d_0 lattice spacing, stress-free lattice spacing (Å)
ε strain
E Young's modulus (GPa)
hkl Miller index
$J_{elastic}$ elastic strain energy release rate (J)
σ applied stress (MPa)
σ_0 yield strength (MPa)
υ Poission's ratio
x, y co-ordinate system (mm)

2. Methodology

2.1. Material and Samples

Fracture tests were carried out, in-situ, at the Diamond Light Source on the I12:JEEP beamline (Drakopoulos et al., 2015), on Al-Ti metal matrix composite (MMC) double edge notch tension (DENT) samples. These samples had varying sample thicknesses (b) and crack lengths (a); this test matrix was chosen to allow for the assessment of varying levels of 3D plastic constraint on fracture and is detailed in Table 1. This research is still ongoing and the initial results for the two thinner specimens ($b = 5$ mm) are presented here alongside the novel measurement methodology and analysis approach. The experimental setup and sample geometry can be seen in Figure 1.

Testing was carried out on a 10 kN Shimadzu loading frame, which was mounted in Experimental Hutch 2 (EH2), which was designed to accommodate large experimental setups. The fracture behaviour was interrogated through a combination of (a) XRD and (b) XCT or, more specifically, through the associated use of digital volume correlation (DVC). XRD allows for measurement of through thickness averaged elastic strain, while DVC allows for the characterisation of the total 3D displacement or strain fields as a function of position through thickness. In this paper we will detail the results of the XRD elastic strain measuremeßnts and initial attempts that have been made to model these using the finite element method. Note that while XRD and XCT measurements could not be made simultaneously, the acquisition mode could be switched semi-automatically in under 10 minutes, allowing elastic and total strain measurements to be made under effectively identical conditions. These measurements were carried out at 7 load increments between 50 N and fracture, which occurred at 4.5 kN and 4.0 kN at a/W = 0.1 and a/W = 0.5 respectively.

Table 1. Test matrix for the full program of work, highlighting the in-plane and out-of-plane constraint with respect to sample geometry and crack length. The tests highlighted in green are the subject of the current paper.

	b = 5 mm	b = 20 mm
a/W = 0.1	Low in-plane Low out-of-plane	Low in-plane High out-of-plane
a/W = 0.5	High in-plane Low out-of-plane	High in-plane High out-of-plane

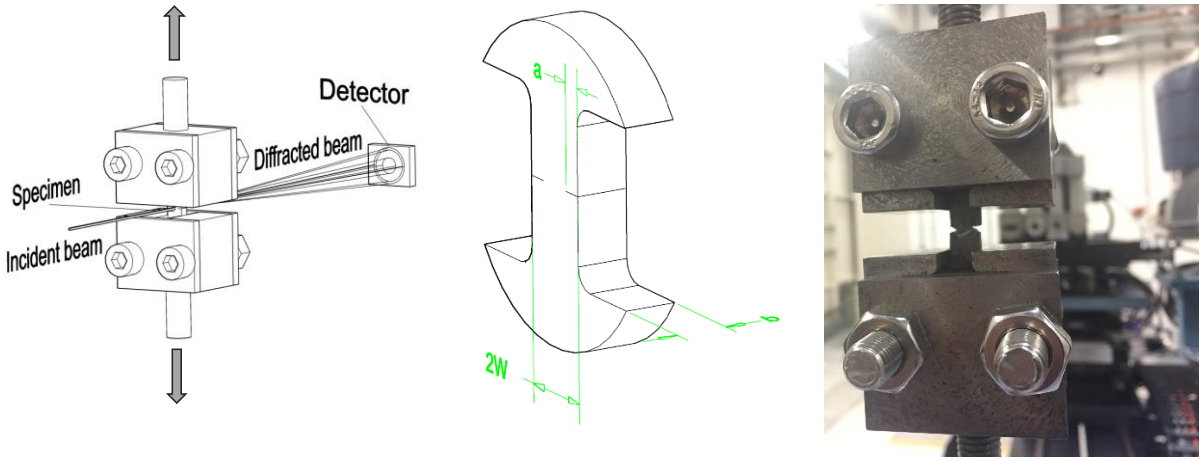

(a) (b) (c)

Fig. 1. Overview of the experiment setup. (a) Schematic view of the loading details and detector/transmission geometry; (b) DENT specimen where a is the crack length, W the width and b its thickness; (c) a fractured specimen inside the loading jig at EH2

2.2. Synchrotron X-ray Diffraction

Monochromatic XRD was used to measure the elastic strain distribution in the Al-Ti MMC samples using a 2D Thales Pixium RF4343 area detector (2881 x 2880 pixels) and a beam energy of 60 keV. The sample to detector distance of 1.5 m allowed for a maximum diffracted angle, 2θ = 8˚ and the acquisition of seven Al peaks and four Ti peaks. Diffraction patterns were acquired using an incoming slit size of 0.1 mm square. The initial pre-processing of the data leveraged the DAWN analysis suite (Filik et al., 2017), with the Debye-Scherrer rings being azimuthally integrated across 5˚ windows. At each loading stage and for both the sample at (a) a/W = 0.1 and (b) a/W = 0.5, diffraction data was acquired across a 2D grid. Each map consisted of approximately 500 points across an area 8 mm x 4 mm with a point spacing of 0.3 mm. In the area surrounding the notch tip, the point density was higher, with an associated spatial resolution of 0.15 mm. The increase in spatial resolution was chosen to better capture the high strain gradient observed in this region. An example of the integrated diffraction pattern can be seen in Figure 2.

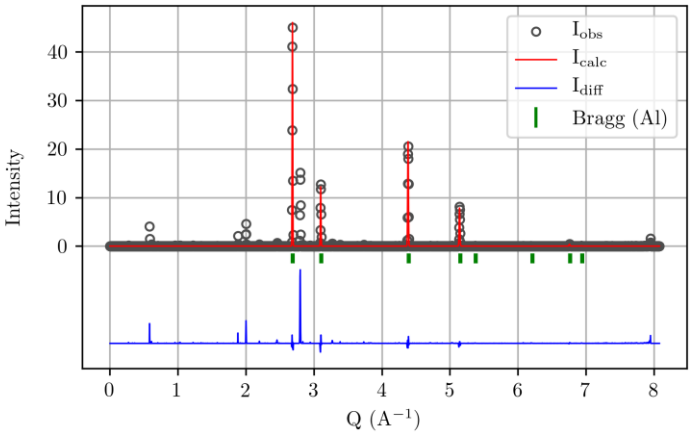

Fig. 2. Diffraction pattern acquired from the Al-Ti MMC. The red line which overlays the integrated diffraction data highlights a Pawley refinement on the Al peaks. The unfitted peaks correspond to reflections from the Ti particles.

2.3. Finite element analysis

A 3D finite element model replicating the sample and test set-up was built using the Abaqus finite element software. Two planes of symmetry were used to reduce the volume of the sample to a quarter of the actual size; x and y symmetry boundary conditions were enforced on the planes of symmetry at the edges of the model. This enabled the number of elements to be reduced by a factor of 4. There were two parts: a 3D rigid body, representing the loading fixture and a 3D deformable solid representing the sample. Load was applied on the rigid body in displacement control such that the correct load was achieved (as per the loads shown in Figure 6). The displacement was applied at a rigid body reference point which was in normal contact with the sample defined in the model. The crack was modelled as a contour integral crack in Abaqus. A symmetry half-crack model was used with the crack tip being along the same line as the crack front. The vector specifying the direction of crack extension was perpendicular to the surface of the notch. No degeneracy or collapsed nodes were used in the mesh. All mesh elements in the notch and those under boundary conditions were of equal size. To model the contact, a rigid body was defined to represent the test rig. The test rig was placed in contact with the sample along the outer side under the wing of the sample (see Figure 4). The rigid body was defined as the master and the sample surface as the slave in the surface to surface contact. The normal behaviour was defined as being in hard contact and the tangential behaviour was frictionless. No slave adjustment or surface smoothing was applied. A Ramberg-Osgood model was used to simulate elastic-plastic behaviour. This model uses the summation of the elastic and plastic components of strain. The parameters used were E = 100 GPa, v = 0.3, n = 6, σ_0 = 103 MPa, α = 2.75, where E is the Young's modulus, v the poisons ratio, σ_0 the yield strength, and n and α describe the hardening behaviour of the material. The values were selected by fitting the Ramberg-Osgood material model (Eq. 1) to a tensile test carried out on the material using a flat dog bone specimen according to ASTM E8M-16A (ASTM International, 2016); this data and the associated fit of the parameters is shown in Figure 3.

$$\varepsilon = \frac{\sigma}{E} + \alpha \frac{\sigma}{E}\left(\frac{\sigma}{\sigma_0}\right)^n \qquad \text{Eq. 1}$$

The edges that represent axes of symmetry were fixed along x and y symmetry boundary conditions (see Figure 4 for the coordinate system). The model used linear, 3D stress elements from the standard Abaqus library. Reduced integration was enabled, but second-order accuracy was not allowed. There were 14,830 elements used to mesh the

sample. The short and long crack models are depicted in Figure 4. To allow for comparison with the experiment data, the linear elastic strains in the crack (notch) opening direction were extracted.

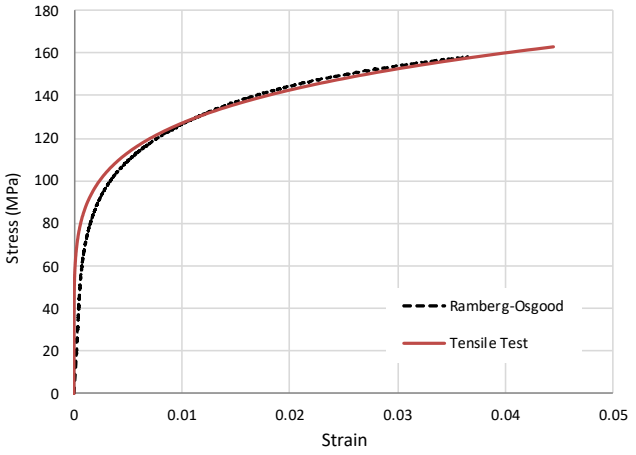

Fig. 3. The stress-strain curve for the Al-Ti MMC employed as part of this study and associated Ramberg-Osgood fit

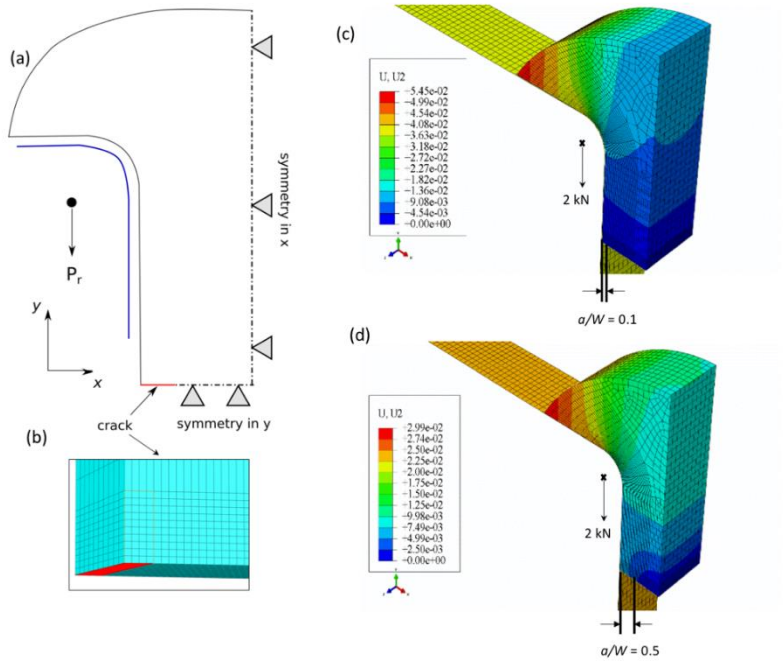

Fig. 4. (a) The FE model boundary conditions and (b) the finite element mesh around the crack tip for a/W = 0.1. The line running along the inner wing of the sample shown in (a) highlights the modelled rigid body contact and displacement (representative of the test rig), resulting in a reaction force, P_r. (c – d) The displacement fields and mesh overview for the thin (b = 5 mm) samples with a short and long notch, such that (c) a/W = 0.1; (d) a/W = 0.5. The noted reaction force of 2 kN is representative of experimental loading to 4 kN due to the symmetry boundary conditions.

3. Results and Discussion

3.1. Elastic strain fields (XRD)

A multi-peak, Pawley refinement was used to evaluate the peak shifts and associated strain with respect to load in the Al matrix using the pyXe strain analysis package (Simpson, 2016). The Pawley refinement of the Al matrix is overlaid on the integrated diffraction profile shown in Figure 1, with the unfitted peaks corresponding to reflections associated with the Ti particles. Strain was calculated from peak shifts relative to a strain free, far field measure of the lattice parameter, d_0 (Withers, Preuss, Steuwer, & Pang, 2007) measured at minimum load such that $\varepsilon = (d - d_0) / d$. Further details of the diffraction analysis procedure can be found in the work of Mostafavi et al. (Mostafavi et al., 2017). Two examples of the 2D elastic strain field maps can be seen in in Figure 5; these detail the elastic strain field at 4 kN when a) a/W = 0.1 and b) a/W = 0.5. Line profiles were also extracted from these maps using 2D linear interpolation, with the lines being taken coincident with the centre of the notch, where y = 0. The line profiles, shown as a function of applied load, can be seen in Figure 6. As noted, the strain maps and associated line profiles detail the strain in the Al matrix; as part of the broader study, efforts will be made to calculate the elastic strain from the Ti particles. This will allow the load partitioning between the two phases to be assessed. Work is also ongoing to determine the elastic component of the strain energy release rate, $J_{elastic}$ from the 2D strain maps using JMAN_S (Barhli et al., 2016). JMAN_S uses Cholesky factorisation to calculate the displacement field from the in-plane strain tensor field. The displacement field (and the associated stress field) are then used to calculate $J_{elastic}$ via a contour integral approach.

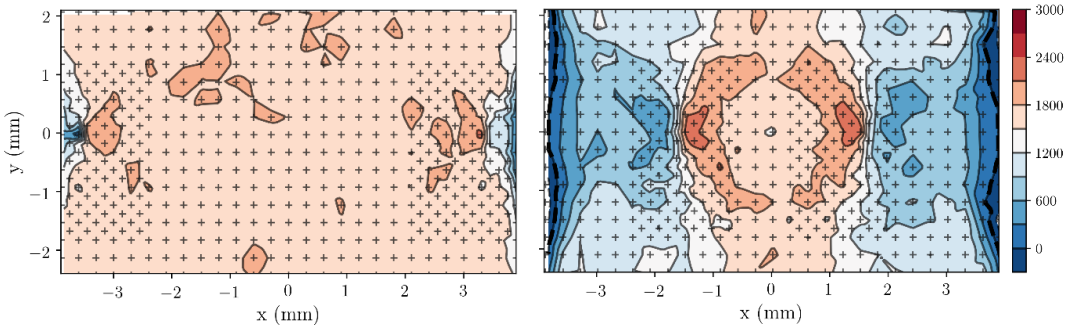

Fig. 5. 2D elastic strain (ε_{yy}) fields acquired using XRD at an applied load of 4 kN for (a) a/W = 0.1; (b) a/W = 0.5.

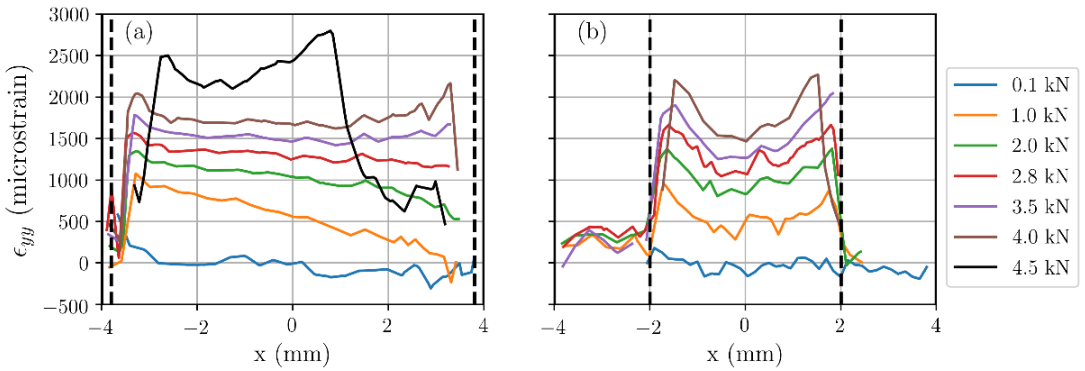

Fig. 6. Line profiles extracted from the 2D elastic strain maps as a function of load at (a) a/W = 0.1; (b) a/W = 0.5.

3.2. FEA vs. Experimental Comparison

A comparison between the experimental and modelled full field elastic strain (ε_{yy}) is shown in Figure 7 for both the (a) short (a/W = 0.1) and (b) long (a/W = 0.5) notch specimens. Line profiles at y = 0 mm have also been extracted and compared for both samples at loads ranging from 1 kN to 4 kN – these can be seen in Figure 8. In the sample with a short notch and low levels of plastic constraint, the modelled and experimental work do not show the desired level of agreement. In the region close to the crack tip, the FEA modelled strain is much greater in magnitude than the experimentally measured results (> 1000 microstrain higher at an applied load of 4 kN), and, while less severe, the disagreement between measured and predicted strain in the far field is still significant. A comparison between the mid thickness (i.e. x = 0 mm) measured and predicted strains can be seen in Figure 9; the FEA modelled strains are between 250 and 450 microstrain greater than the measured results. Furthermore, the general shape of the strain field is not well matched, with a dip in strain being predicted approximately 0.5 mm ahead of the crack tip – this is not observed in the experimental work. The agreement between FEA and XRD is, however, better for the long notch and, while the strain field near the notch is still seemingly overpredicted, the far field strains are very closely matched (<100 microstrain difference) and the overall strain field distribution is similar to the experimentally recorded field.

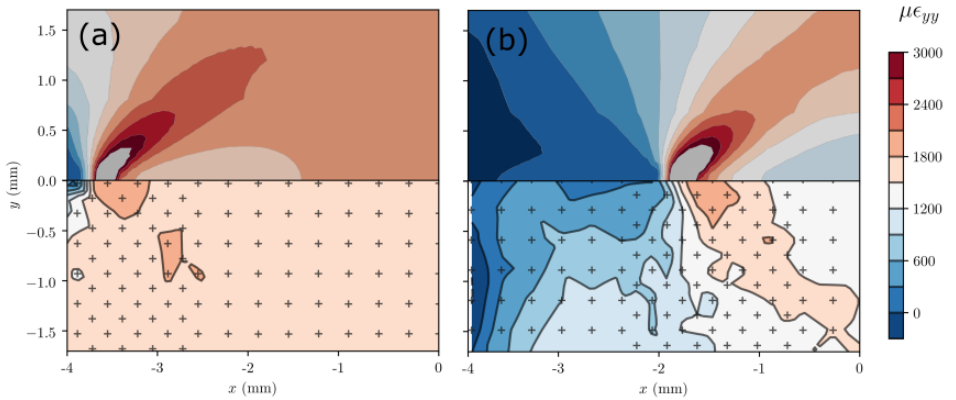

(a) (b)

Fig. 7. A comparison of the FEA (top) and experimental (bottom) elastic strain, ε_{yy} at (a) a/W = 0.1; (b) a/W = 0.5. The region in grey highlights regions that exceeds 3000 microstrain in the FEA analysis.

The difference between the experimental and modelled results in the region close to the tip of the electro discharge machined notch can be attributed to at least three factors. The first two are imposed by the experimental set-up and, more specifically, the resolution of the measurements. XRD spatial resolution is a feature of (a) the point spacing in the acquisition grid (in this case approximately 150 µm) and (b) the geometry of the gauge volume, which is a function of the slit size and acquisition mode. In this case a 100 µm x 100 µm slit size was used with a monochromatic, pencil beam setup. The result of this is that the strain measurements are not discrete points but averaged across a volume 100 µm x 100 µm x 4000 µm. Averaging through thickness increases measurement sensitivity to (a) sample misalignment or non-straight crack fronts and (b) changes in stress state/constraint through thickness (i.e. plane stress tending toward plane strain). Inaccuracies introduced by low spatial resolution are particularly acute where the strain gradient is high

e.g. near a notch or crack tip. Spatial resolution should ideally well match with the strain gradient but this is clearly limited by physical and experimental feasibility (which this experiment approached the limits of) and is not possible in the presence of a sharp defect.

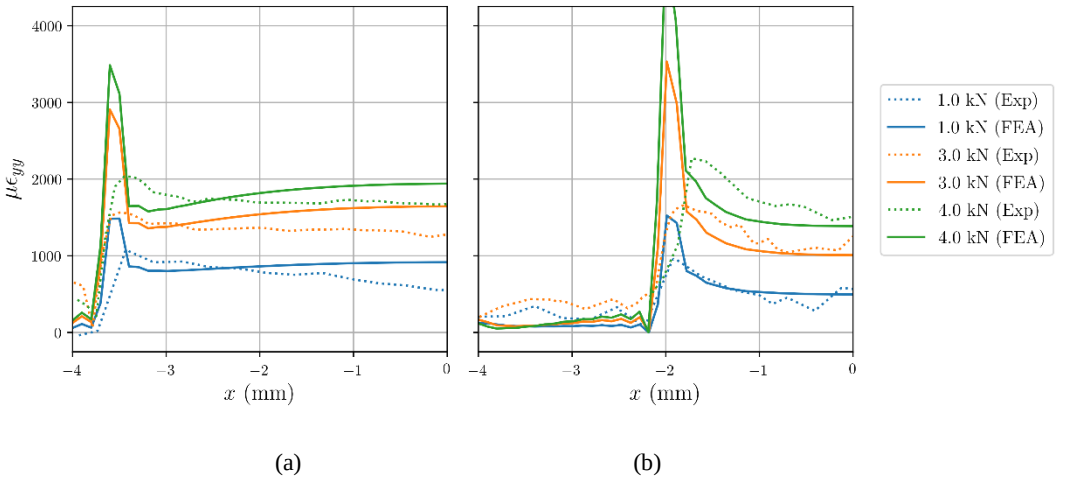

(a) (b)

Fig. 8. A comparison of line profiles extracted from the 2D elastic strain maps as a function of load at (a) a/W = 0.1; (b) a/W = 0.5.

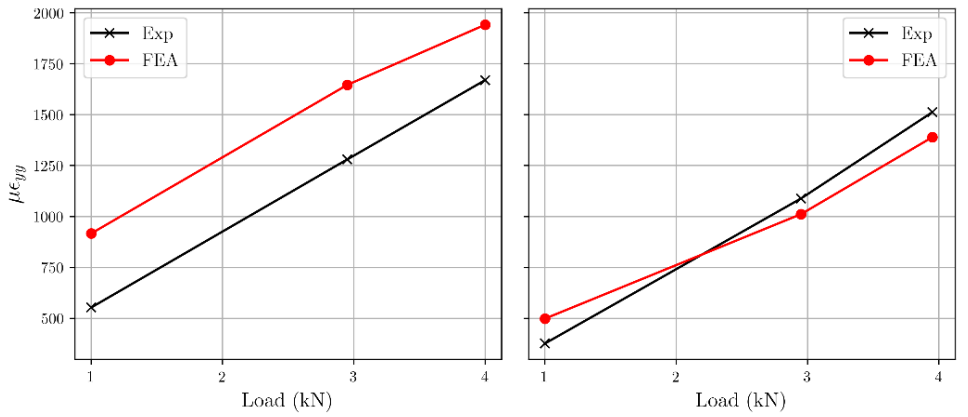

(a) (b)

Fig. 9. A comparison between experimental and modelled elastic strain at mid thickness (x = 4 mm) for (a) a/W = 0.1; (b) a/W = 0.5.

In addition to experimental factors, the authors consider it likely that much of the discrepancy can be explained by the manner in which the notch is treated in the FE model. It is currently modelled and meshed as a sharp defect, rather than a blunted notch; the results from the X-ray computed tomography (to be published separately) suggest this is incorrect, with significant blunting being observed. The FE model would therefore be expected to predict a strain and stress excursion that broadly approximates to the elastic portion of a HRR field i.e. power law hardening material, with stresses asymptotically increasing towards the notch. While the strain fields may not agree in this region, it is

expected that they would converge in the far field, where the impact of this non-optimised mesh is no longer significant. This is precisely the behaviour seen where a/W = 0.5 but not, as noted, where a/W = 0.1. The lack of constraint in the sample with the short notch will allow for more plasticity and could introduce errors in the model due to geometric non-linearity. In future iterations of the finite element model allowances will be made for this.

4. Conclusions

In this paper we have highlighted the initial elastic strain field results from a comprehensive experiment, which has leveraged developments in measuring elastic and elastic-plastic deformation fields using synchrotron X-ray diffraction and tomography. The through-thickness averaged elastic strains have been measured and compared against the linear elastic strains extracted from a 3D elastic-plastic finite element model. High energy X-ray diffraction has been shown to be a valuable tool for the validation of finite element models such as these and has highlighted some potential inaccuracies in the described model, which will be addressed in future work. Notably, while there is an acceptable agreement in the far field strains (particularly where a/W = 0.5), further work is required to improve the accuracy of the model to better represent the behaviour in the area around the tip of the notch, which does not currently capture blunting of the notch during loading and overpredicts the strains in this region. Using the volume of the plastic region in each sample, a measure of the level of 3D constraint of the plastic zone can be derived. This will enable the level of constraint to be characterized and a comparison can be made with the J-integral, a measure of the crack driving force for each level of constraint.

Acknowledgements

We thank Diamond Light Source for access to beamline I12 (EE12606-2) that contributed to the results presented here. We would also like to thank Prof. Andrew Sherry and Mr Rajesh Patel, National Nuclear Laboratory for their insight in this project. MM and ST gratefully acknowledge the financial support by NNL through an Industrial Case studentship.

Appendix A. Supplementary material

The integrated X-ray diffraction intensity profiles and associated elastic strains with respect to applied load can be accessed at https://doi.org/10.5523/bris.2lo01f5ww0vk42dqiq212z5bn5.

References

ASTM International. (2016). *ASTM E8/E8M--16a, Standard Test Methods for Tension Testing of Metallic Materials*. West Conshohocken, PA. https://doi.org/10.1520/E0008

Barhli, S. M., Saucedo-Mora, L., Simpson, C., Becker, T., Mostafavi, M., Withers, P. J., & Marrow, T. J. (2016). Obtaining the J-integral by diffraction-based crack-field strain mapping. *Procedia Structural Integrity*, *2*, 2519–2526. https://doi.org/10.1016/j.prostr.2016.06.315

Drakopoulos, M., Connolley, T., Reinhard, C., Atwood, R., Magdysyuk, O., Vo, N., … Wanelik, K. (2015). I12: the Joint Engineering, Environment and Processing (JEEP) beamline at Diamond Light Source. *Journal of Synchrotron Radiation*, *22*(3), 828–838. https://doi.org/10.1107/S1600577515003513

Filik, J., Ashton, A. W., Chang, P. C. Y., Chater, P. A., Day, S. J., Drakopoulos, M., … Wilhelm, H. (2017). Processing two-dimensional X-ray diffraction and small-angle scattering data in DAWN 2. *Journal of Applied Crystallography*, *50*, 959–966. https://doi.org/doi.org/10.1107/S1600576717004708

Larsson, S. G., & Carlsson, A. J. (1973). Influence of non-singular stress terms and specimen geometry on small-scale yielding at crack tips in elastic-plastic materials. *Journal of the Mechanics and Physics of Solids*, *21*(4),

263–277. https://doi.org/10.1016/0022-5096(73)90024-0

Mostafavi, M., Collins, D. M., Peel, M. J., Reinhard, C., Barhli, S. M., Mills, R., … Connolley, T. (2017). Dynamic contact strain measurement by time-resolved stroboscopic energy dispersive synchrotron X-ray diffraction. *Strain*, *53*(2), 1–13. https://doi.org/10.1111/str.12221

Mostafavi, M., Smith, D. J., & Pavier, M. J. (2010). Reduction of measured toughness due to out-of-plane constraint in ductile fracture of aluminium alloy specimens. *Fatigue and Fracture of Engineering Materials and Structures*, *33*(11), 724–739. https://doi.org/10.1111/j.1460-2695.2010.01483.x

Mu, M. Y., Wang, G. Z., Tu, S. T., & Xuan, F. Z. (2016). Three-dimensional analyses of in-plane and out-of-plane crack-tip constraint characterization for fracture specimens. *Fatigue and Fracture of Engineering Materials and Structures*, *39*(12), 1461–1476. https://doi.org/10.1111/ffe.12461

O'Dowd, N. P., & Shih, C. F. (1991). Family of crack-tip fields characterized by a triaxiality parameter—I. Structure of fields. *Journal of the Mechanics and Physics of Solids*, *39*(8), 989–1015. https://doi.org/10.1016/0022-5096(91)90049-T

Seal, C. K., & Sherry, A. H. (2017). Predicting the effect of constraint on cleavage and ductile fracture toughness using area contour toughness scaling. *Engineering Fracture Mechanics*, *186*, 347–367. https://doi.org/10.1016/j.engfracmech.2017.09.029

Simpson, C. A. (2016, April 21). pyxe: XRD Strain Analysis. https://doi.org/10.5281/zenodo.50185

Withers, P. J., Preuss, M., Steuwer, A., & Pang, J. W. L. (2007). Methods for obtaining the strain-free lattice parameter when using diffraction to determine residual stress. *Journal of Applied Crystallography*, *40*(5), 891–904. https://doi.org/10.1107/S0021889807030269

Yang, J., Wang, G. Z., Xuan, F. Z., & Tu, S. T. (2013). Unified characterisation of in-plane and out-of-plane constraint based on crack-tip equivalent plastic strain. *Fatigue and Fracture of Engineering Materials and Structures*, *36*(6), 504–514. https://doi.org/10.1111/ffe.12019